Unifying the Effects of in and out-of-plane constraint on the fracture of ductile materials

S M Tonge[1], C A Simpson[1], C Reinhard[2], T Connolley[2], AH Sherry[3], TJ Marrow[4], M Mostafavi[1,*]

1. Department of Mechanical Engineering, University of Bristol, Queens Building, University Walk, Bristol, BS8 1TR
2. Diamond Light Source Ltd, Harwell Science and Innovation Campus, Didcot, Oxfordshire OX11 0DE
3. National Nuclear Laboratory, 5th Floor, Chadwick House, Warrington Road, Birchwood Park, Warrington, WA3 6AE
4. Department of Materials Science, University of Oxford, 21 Banbury Road, Oxford OX2 6HT

Abstract

Effects of plastic constraint on the fracture of materials have been studied extensively. Often in such studies, the plastic constraint is divided into in-plane and out-of-plane directions and each treated separately. Such a separation adds considerable complexity to the engineering structural integrity assessment analyses. Despite previous suggestions for unifying the effects of constraint in a single parameter, the current engineering assessments have not been updated due to lack of direct experimental validation of such parameters. In this study, we directly measured the effects of in-plane and out-of-plane constraints, for the first time, in the form of plastic zone around the crack using advanced experimental techniques. The measurement of constraints in four specimens with different levels of in and out of plane constraints, allowed us to show and relate the interdependency of in and out of plane constraints. The tests were carried out using synchrotron X-ray tomography with in-situ loading. Attenuation contrast between the constituents of the metal matrix composite material used allowed the tomograms to be analysed using digital volume correlation which calculated the full-field displacement within the samples. The displacement fields were used via a finite element framework to calculate the energy release rate in the form of the *J*-integral along the crack fronts. The measured plastic zone sizes, dependent on the combined level of in plane and out of plane constraints, were used successfully to rank the *J*-Integral at fracture of the samples. It was therefore proved the level of plastic constraint can be quantified by using the size of the plastic zone as without separating it into two components thus simplifying the treatment of constraint in structural analyses significantly.

1 Background

1.1 Plastic constraint

Plastic constraint has been shown to considerably affect the measured toughness in metallic materials that show limited plasticity before fracture [1]. High constraint specimens such as compact tension and single edge notch bend, with a crack extending to almost half of the ligament with a thickness that satisfies plane strain conditions, are regraded to measure the lower bound fracture toughness [2]. This is because the loss of constraint results in an apparent increase in the fracture toughness due to the higher level of plastic work required before crack

* Corresponding author
Tel: +44 (0) 117 331 5717
Email: m.mostafavi@bristol.ac.uk

initiation [3–5]. Constraint is often divided into in-plane and out-of-plane, where in-plane is along the direction of the crack propagation and out-of-plane is perpendicular to it along the crack front. In-plane constraint is predominantly influenced by the specimen geometry and the crack length, while the major factor in out-of-plane constraint is the thickness. Despite the similarity between the physical effects of in and out-of-plane constraints, they are treated separately in engineering structural integrity assessment codes due to lack of a unified measure of constraint [6], adding complexity to the analysis. Different parameters have been used to quantify in and out-of-plane constraint, which are briefly reviewed below.

1.2 In-plane constraint

The *T*-stress is a second order term of the asymptotic stress field along the crack tip independent of distance from it [7]. It has been shown that *T*-stress is a measure of in-plane constraint when the plastic zone around the crack tip is small enough for the stress field to be reliably approximated by linear elastic fracture mechanics [8]. It is argued that due to the effect of the plastic region on the stress field around a crack, it is not possible to use a single parameter for fracture assessments [9]. For this reason, *T*-stress has been used as an additional parameter to *K*, the stress intensity factor, in fracture assessments [10]. The validity of using *T*-stress as a measure of in-plane constraint is supported by the evidence of a large number of experiments, showing the variation of apparent fracture toughness as a function of *T*-stress [11][12]. The sign of the *T*-stress as well as its magnitude indicates the size of the plastic zone which varies as the in-plane constraint changes [13]. Fracture toughness and the size of the plastic zone around the crack tip increases with increasing negative value of *T*-stress. Zero and small positive values of *T*-stress, as obtained in the standard fracture toughness specimens, are considered to minimise the size of the plastic zone around the crack tip thus resulting in the lower bound fracture toughness [14]. A more positive *T*-stress, however, can cause crack instability and branching [15]. *T*-stress is also sensitive to the loading regime; for example, in a single edge notch specimen under tensile loads the *T*-stress will be negative, while it will switch to a low positive value for a bending load. To enable fracture assessments to take the effects of constraint into account, *K* - *T* loci have been constructed empirically [16]. In order to expand the applicability of elastic *T*-stress to elastic plastic conditions, *J* - *T* loci have also been compiled (*J* is the *J*-integral, energy release rate associated with a crack in a nonlinear elastic medium) [17][18].

While *T*-stress is a valid measure of in-plane constraint for materials with near linear elastic behaviour, Q is used in the case of elastic-plastic materials. It was defined by O'Dowd and Shih [19][20] as shown in (Eq. 1).

$$\sigma_{ij} = \sigma_{ij}^{HRR} + Q\sigma_o\delta_{ij} \qquad \text{(Eq. 1)}$$

σ_{ij} is the measured/simulated stress field around the crack tip, σ_{ij}^{HRR} is the stress field as defined by Hutchinson, Rice and Rosengren [21,22] (HRR) for a nonlinear elastic material (e.g. Ramberg-Osgood material model) and σ_0 is the material yield stress. Q can be seen as the difference, at any point in the stress field, between the stress field as defined by HRR whose magnitude is quantified by the *J*-integral (J) and the measured/simulated stress field. It thus quantifies the deviation from the stress field in high constraint standard specimens. The implementation of Q into the assessment codes uses the definition given in (Eq. 2.

$$Q = \left.\frac{\sigma_{yy} - \sigma_{yy}^{SSY(T=0)}}{\sigma_0}\right|_{r=\frac{2J}{\sigma_0}} \qquad \text{(Eq. 2)}$$

Q is given at a radial distance $r = 2J/\sigma_0$. σ_{yy} is the opening stress (see Figure 1a for the coordinate system) r is the radial distance from the crack tip, and $\sigma_{yy}^{SSY(T=0)}$ the opening stress for the small scale yielding condition when T-stress is zero. When Q is negative, the stress field expirenced by the material is lower than the predicted reference stress field. When the stress field is greater than the reference stress field, the Q value is positive. Therefore, similar to T-stress, negative Q shows the loss of constraint and an increase in the apparent fracture toughness while positive Q indicates high in-plane constraint resulting in the measured lower bound fracture toughness. Experiments to measure and tabulate Q showed that it was possible to greatly increase the scope of assessments using J by also including the Q parameter [23]. J - Q loci have been produced which are incorporated in the assessment procedures such as R6 [24] and BS7910 [25]. Further evaluation of J - Q theory has been performed for specific samples including single edge notch bend (SENB) and compact tension specimens [26] and new formulae were proposed to optimise the calculation of Q in a situation with high plastic deformation for bending samples [27].

It is also argued that Q quantifies the triaxiality of stress around the crack tip [2]. The stress triaxiality factor (T_f) is the ratio of the hydrostatic stress to the von Mises stress and relationships between Q and T_f have been proposed [28]. Alternatively, T_f has also been used to quantify constraint and include it in the assessment procedures [29]. Other measures of constraints have also been proposed such as A_2 [30] which are somehow analogous to Q.

1.3 Out-of-plane constraint

T-stress and Q quantify in-plane constraint while T_z is the out-of-plane constraint factor [31]. It has been defined in (Eq. 3, in terms of different components of a stress field [9].

$$T_z = \frac{\sigma_{zz}}{\sigma_{xx} + \sigma_{yy}} \qquad \text{(Eq. 3)}$$

It is defined for a crack plane occupying the xz plane and propagating along the x direction. The motivation for using T_z is similar to the other two-parameter approaches (e.g. K - T and J - Q), in this case taking into account the effect of out-of-plane constraint (predominantly component thickness). To gain information about out-of-plane constraint, finite element simulations can be used to find T_z in a range of different thicknesses with similar in-plane geometry. Originally, Guo used simulations of elastic plates with embedded centre-elliptical cracks and considered different aspect ratios (i.e $0.2<a/c<1$ where a is the crack depth and c is its surface length) to quantify T_z. The results were used to propose a two-parameter theory K - T_z that accounts for out-of-plane constraint [9]. To combine the effects of in and out-of-plane constraint, three parameter theories such as K - T - T_z and J - Q - T_z have been proposed [32][33]. Comparisons were made between K - T - T_z, J – Q - T_z and K - T and J - Q theories which showed that the proposed three dimensional methods were able to account accurately for three-dimensional stress fields [34] though they are complicated and require large experimental datasets in which both in-plane and out-of-plane constraints vary.

1.4 Unified measure of constraint

Although many of the parameters quantifying constraint are restricted to either in or out-of-plane, there are parameters that are sensitive to both forms of constraint. It is therefore possible that a loci of fracture toughness could be found from a two-parameter fracture assessment by combining the effects of constraint regardless of its direction. For example, Dodds, Anderson and Kirk [35] proposed using the area inside a contour defined by an arbitrary constant maximum principal stress as a measure of constraint (see (Eq. 4 [36]).

$$\frac{\sigma_1}{\sigma_0} = C \qquad \text{(Eq. 4)}$$

C is an arbitrary constant, σ_1 and σ_0 are the maximum principle stress and the yield stress respectively. The size of area bounded by the contour (A_c) determines the level of constraint. High constraint results in a smaller area while low constraint yields a larger area [37]. Therefore, a dimensionless parameter φ, defined in (Eq. 5, is suggested as a unified measure of constraint:

$$\varphi = \frac{A_c}{A_c^{SSY}} \qquad \text{(Eq. 5)}$$

φ is the ratio between the area confined within an arbitrary isostress contour C (A_c) to the area measured when small scale yielding prevails (i.e. A_c^{SSY}) [38]. While this parameter can be used for the fracture of ductile materials which show small scale yielding, it is no longer applicable when large scale plasticity occurs. For this reason, variations of the Dodds, Anderson, Kirk method have been proposed; for example, Mostafavi and co-workers suggested φ^p [39].

$$\varphi^p = \sqrt[3]{\frac{V_P}{V_{ref}}} \qquad \text{(Eq. 6)}$$

where V_P is the volume of the plastic zone in a given component and V_{ref} is the volume of the plastic zone in a standard high constraint specimen (e.g. compact tension). While it was shown that φ^p can predict the failure of aluminium alloys in combined in and out-of-plane constraint condition [38], its application is limited to component geometries and loads in which the plastic zone size is a small proportion of the uncracked ligament, i.e. contained. Yang et al. proposed another modification to the Dodds, Anderson, Kirk method in which A_{PEEQ}, the plastic strain volume within a ε_p isoline, is normalised by A_{ref} which is the volume within the isoline for a sample with high constraint [40].

Studies testing the effect of in- and out-of-plane constraint on a large number of parameters have been carried out. Shlyannikov et al. showed that the stress intensity factor changes as both in- and out-of-plane constraints change [41]. Mu et al. carried out finite element simulations on a series of compact tension and single edge notch bend specimens with varying in and out of plane constraints; they found that φ responded to changes in both in and out-of-plane constraints well [42]. This could allow the use of A_p as a unified constraint parameter in future. Seal and Sherry have recently combined the Rice and Tracy [43] fracture criterion with the φ constraint parameter to predict the effects of fracture of ductile materials [44].

Recently different variations of Anderson – Dodds – Kirk unified measure of constraint have been considered and theoretical investigation on their validity has been performed (e.g. see [45,46]). For example, a CTOD based unified measure of constraint, A_p, has been developed [47] similar to Anderson – Dodds – Kirk concept. Based on these theoretical studies, A_p – toughness loci have been built for brittle [48] and ductile [40] materials as well as weldments [49] or similarly A_d – toughness loci are built for pipes [50].

While it is shown that the normalised plastic volume near the crack tip in various forms can be used as a unified measure of constraint, potentially simplifying the methods that account for the constraint effect, they have not been included in assessment procedures yet. This is partly

due to limited validation of the methods, since measuring full-field strains and the volume of plasticity around the crack tip has not been possible except on the surface of the material (e.g. using optical methods such as digital image correlation [51]). In this work, we employed advanced measurement techniques, namely X-ray tomography and Digital Volume Correlation, to make such measurements for the first time.

2 Experiments and Results

2.1 Specimens and material

The purpose of this work is to directly measure the energy release rate and the size of the plastic region developed around the crack tip upon crack initiation. The measurements will be used to validate unified measures of constraint. To this end, double edge notch tension specimens (see Figure 1a) were tested; the specimens had cracks with an initial length a, width W and thickness b. It has been shown before that for materials that show large crack tip blunting before fracture (e.g. aluminium alloys [52]), fatigue pre-cracking is not necessary. Thus, wire electro-discharge machining with a 0.1 mm wire diameter was used to introduce a sharp notch/crack in the samples. Grips were designed to attach the specimen to the test frames (see Figure 1b).

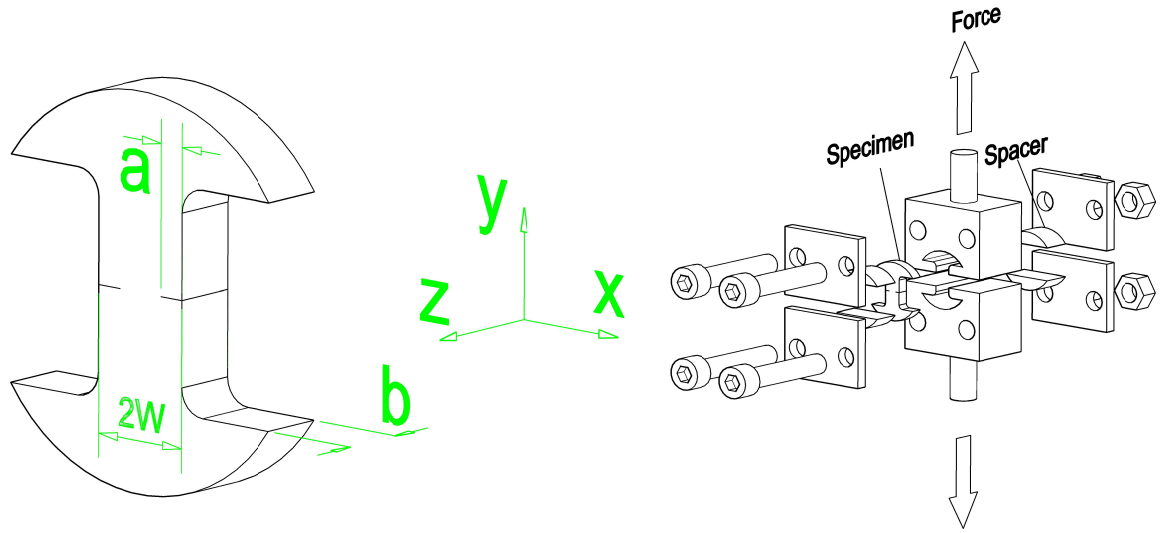

Figure 1: Test specimen (a) the fixture connecting the sample to the loading frame (b) single edge notch tension specimen

Four different samples with varying in and out-of-plane constraint levels were tested. Different thicknesses were used to vary the level of out-of-plane constraint (b = 5 and 20 mm). Different notch lengths were used (a = 0.4 and 2 mm) to provide different levels of in-plane constraint. Details of the samples can be seen in Table 1.

The applicability and quality of Digital Volume Correlation data is strongly dependent on the size and distribution of the inherent, internal speckle pattern [53]. It was therefore necessary to select a material containing microstructural features with distinct X-ray attenuation coefficients with respect to their matrix; this would provide an appropriate speckle pattern with sufficient contrast in the tomograms. To this end a metal matrix composite with an aluminium matrix and titanium particles was selected. The difference between attenuation contrast of

aluminium (0.273 cm^2/g and 0.257 cm^2/g at 59.6 keV and 61.9 keV respectively) and titanium (0.742 cm^2/g and 0.664 cm^2/g at 59.6 keV and 61.9 keV respectively) was sufficient to obtain tomograms with a suitable speckle pattern (see next section for details and choice of X-ray beam energy). The mechanical response of the material, henceforth referred to AlTi, was measured according to ASTM E8 [54] using a 12.5 kN hydraulic testing frame and a round bar specimen. The load was recorded from the frame's load cell which was synchronised through a Vishay System 9000 data acquisition system with the strain measured by a rosette strain gauge. A typical stress – strain curve obtained can be seen in Figure 2. Since no unloading took place in the experiment (see section 2.2), a nonlinear elastic material model, namely Ramberg – Osgood, was used as defined in (Eq. 7) to describe the material properties.

$$\frac{\varepsilon}{\varepsilon_0} = \frac{\sigma}{\sigma_0} + \alpha\left(\frac{\sigma}{\sigma_0}\right)^n \qquad \text{(Eq. 7)}$$

σ_0 is yield stress, ε_0 is yield strain, n is the hardening exponent, and α is a dimensionless offset constant [55][56]. The material has a Young's modulus, E= 100.2 GPa, and n= 6, σ_0= 103 MPa, α= 2.75.

Table 1- details of 4 tested specimens

Name	Thickness b (mm)	Crack length a (mm)	Width $2W$ (mm)	Fracture load F_c (kN)
Short – Thin	5.0	0.4	8	4.5
Long - Thin	5.0	2.0	8	4.0
Short - Thick	20	0.4	8	14.9
Long - Thick	20	2.0	8	15.0

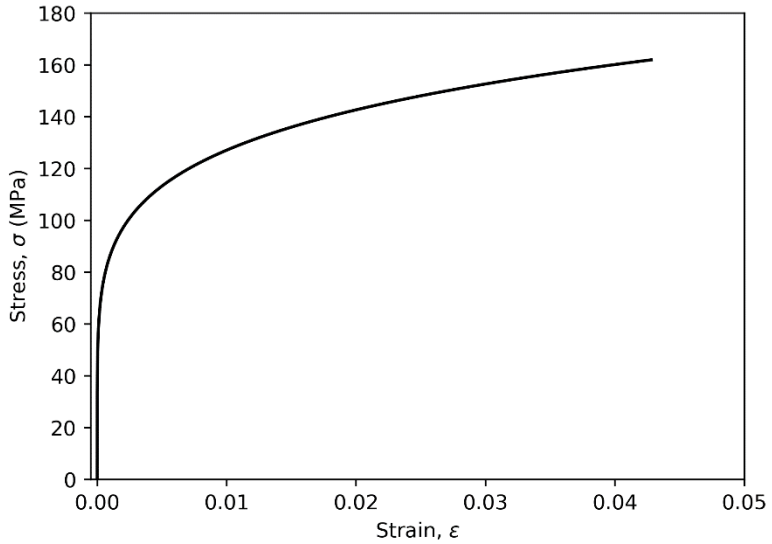

Figure 2: Mechanical response of AlTi

2.2 X-ray computed tomography

The experiment was carried out in Experimental Hutch 2 (EH2) of the I12 beamline at the Diamond Light Source [57] (experiments EE12606-1 and EE12606-2). A 10 kN Shimadzu electric test frame was used to load the 5 mm thick samples and a 100 kN hydraulic Instron test frame was used for the 20 mm thick specimens (these required a higher load than the capacity of the Shimadzu). A view of a fracture specimen within its grip is shown in Figure 3.

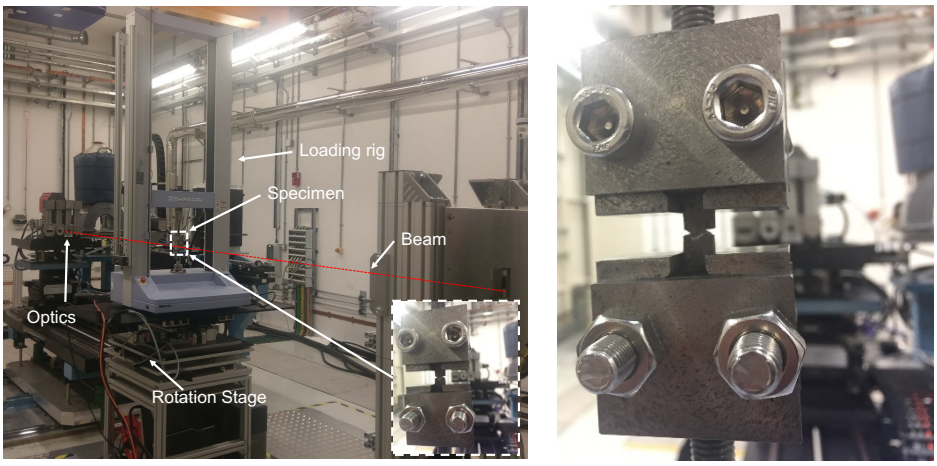

(a) (b)

Figure 3: Experimental setup (a) 10kN loading frame on I12's external experimental hutch tomography stage (b) view of the specimen within the fixture attached to the loading frame

Limited angle computed tomography was performed on all 4 samples (over an angular range of 145˚); this was necessary as the frames of the two-column loading rig design restricted the angles over which radiographs could be acquired. A beam energy of 59.6 keV was employed for the thick samples and 61.9 keV for the thin samples during EE12606-1 and EE12606-2 respectively. For each tomogram 2501 projections were collected using the I12 X-ray imaging modules, utilizing a pco.Edge 5.5 camera at an exposure time of 0.05 s. The projections are observed using optical modules that observe a scintillator, with a resolution that depends on the optical module. Optical module 3 was selected for the thin specimens; this module provides a X2 magnification (i.e. pixel size 3.3 μm^2) with a field of view of 8.0×7.0 mm^2. While the thin samples' full width was within the field of view, the diagonal length (9.4 mm) extended beyond this and thus the sample corners were not captured in the reconstructed tomogram. Optical module 2 was used for the thick specimens; this module has X1 magnification (pixel size 7.9 μm^2) with a field of view of 20×12 mm^2. The thick samples' diagonal lengths were also larger than the field of view thus their corners were similarly missed in the tomograms. The distance between the detector and the specimen was ~1480 mm in all cases. The distance between the specimen and the detector enhanced the phase contrast of the tomograms [58] which helps with crack detection [59].

Initial tomograms were recorded at 50 N (to settle the specimen in the grip but apply minimal load). The specimens were then loaded at 0.1 mm/min in small loading steps while real time radiograph projections were recorded. Once crack initiation was observed in the projection, a full tomogram was recorded with the specimen under load. The 3D tomograms were reconstructed using a Fourier grid reconstruction algorithm (Gridrec) [60], which is implemented in Tomopy [61] and allows for the interpolation of the missing projections (i.e. accounts for the limited angular data). The reconstruction was completed after a sequence of

pre-processing steps, which included a flat-field correction, de-zinger and ring artefact removal [62]. The quality of the reconstructions was high, despite the use of limited angle tomography. The focus of study was on performing Digital Volume Correlation (DVC) to track the movement of material using the internal grey scale features, which was not impaired by limited angle tomography. The reconstructed dataset was 2160 16-bit virtual *xz* slices of the specimens each measuring 2560×2000 pixels; an example series of the image slices is shown in Figure 4a. A representative slice before and after loading is shown in Figure 4b.

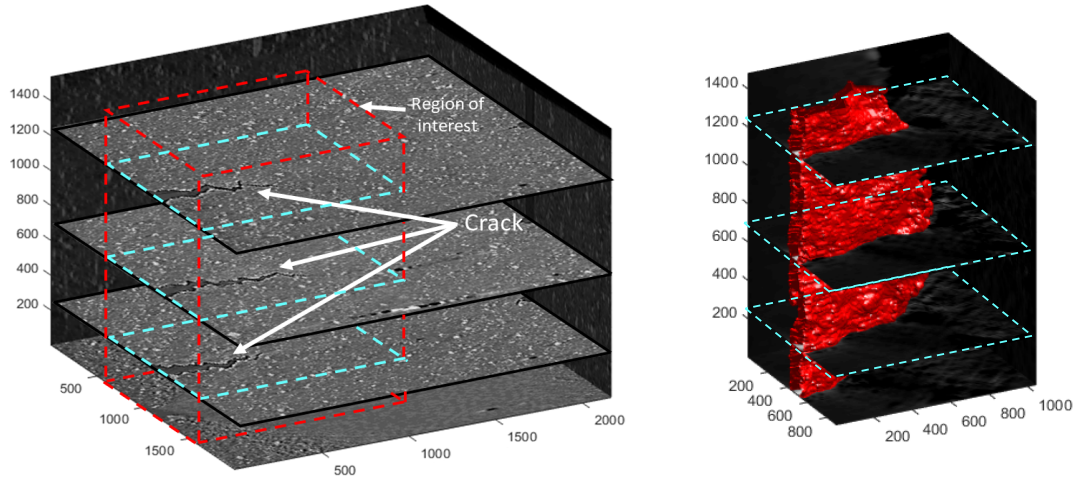

(a)

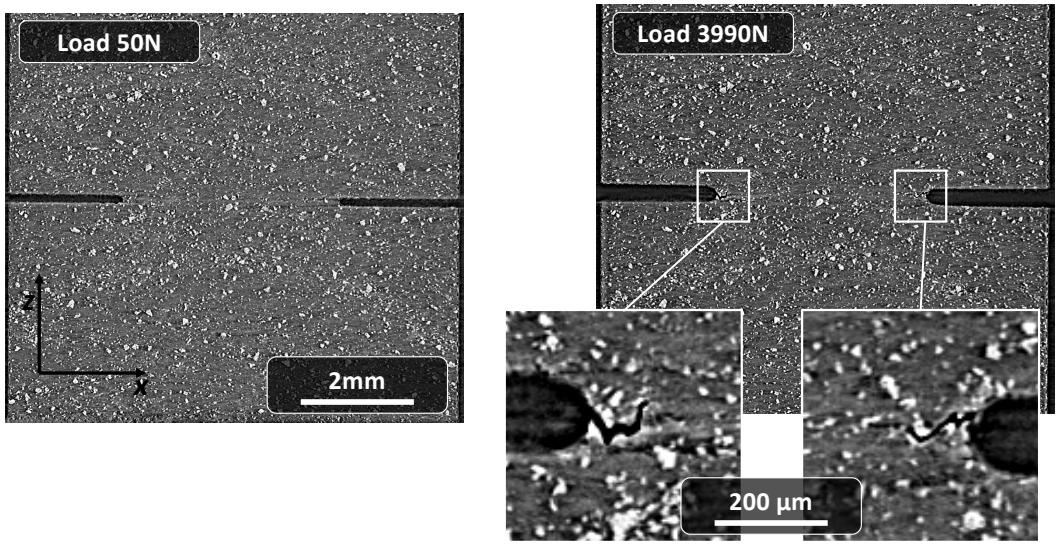

(b)

Figure 4: Reconstructed tomography data (a) virtual stack of xz slices of the cracked thick-long sample and the segmented crack shown in red; each voxel is 3.3µm (b) example of the xz slice before and after cracking in thin long sample at its mid-thickness

2.3 Digital Volume Correlation (DVC)

After the tomograms were reconstructed, each set of reference (50N applied load) and cracked volumetric tomography images for the four conditions of constraints were analysed using DVC. DVC tracks pattern of the grey scale features within the material to build 3D full-field

displacement volumes [53]. The LaVision Davis 8 [51] software was used in this work, employing a cross correlation algorithm in Fourier space (direct correlation using a root mean square minimisation algorithm is available in the newer versions of the software but was not available at the time) [63]. The software divides each tomogram into smaller cubic interrogation volumes and measures their relative movement thus quantifying deformation as a displacement field. To improve the spatial resolution of the full-field displacements the software can start with large interrogation volumes, also known as subsets, which contain more features before splitting the volume into smaller volumes in subsequent passes. Overlaps between adjacent interrogation volumes can also be used to improve the spatial resolution of the displacement field, if the gradients of displacement are sufficiently small. To increase the speed of the analysis, visual inspection of the tomograms was used to identify the region of interest (i.e. the location of the crack - see Figure 4a) and cropping the original 2560×2160×2000 (x×y×z) image stack into smaller stacks. The thick sample with a long crack was cropped to 2200×1550×1500 and then analysed with DVC. The first pass had a subset size 64^3 voxels with an overlap of 50%. The second pass used a subset size of 32^3 voxels with an overlap of 50%. In the third pass a subset size of 16^3 voxels was used with an overlap of 80%. The thick sample with a short crack was first cropped to 2000×1550×1400, then analysed with a subset size 121^3 voxels with an overlap of 80% as the first pass. The second pass used a subset size of 64^3 voxels with an overlap of 50%. In the third pass a subset size of 32^3 voxels was used with an overlap of 50%. In the fourth pass a subset size of 16^3 and overlap of 80%. The thin sample with long notch was not well positioned relative to the beam and the initiated crack was towards the upper side of the image stack rather than its middle. In this case, the stack was be cropped to 300×1550×300 prior to a DVC analysis which started with a subset size 32^3 voxels with an overlap of 50%. A second pass used a subset size of 16^3 voxels with an overlap of 80%. In the third pass a subset size of 8^3 voxels was used with an overlap of 80%. Finally, the thin sample with a short crack was cropped to a size of 1050×1550×900; the DVC analysis started with a first pass a subset size 256^3 voxels with an overlap of 80% was used. The second pass used a subset size of 64^3 voxels with an overlap of 80%. In the third pass a subset size of 32^3 voxels was used with an overlap of 80%. In the fourth pass a subset size of 16^3 voxels was used and an overlap of 50%.

The results of the DVC analyses were four sets of full-field displacement vectors each corresponding to an initiated crack under varying in and sets of out-of-plane constraint conditions. A previously developed code that identifies a crack in a displacement field using a volumetric phase congruency algorithm was used to segment the crack [59][64]. The code also identifies the vertical displacement on either side of the crack face and, by subtracting them from each other at every point across the crack profile, calculates the crack opening displacement along the crack face. An example of the segmented crack (the red volume) is shown in Figure 4a. The results of crack opening displacement calculations can be seen in Figure 5 for each sample. Crack opening displacement along the full thickness of the thin samples could be measured across the sample barring regions very close to the sample edge. The thick samples, however, could not be analysed through the full thickness. This was partly due to their larger diagonal length and an offset between the sample centre and the tomography rotational axis. In order to increase the evaluate the robustness of the complex methodology with which the crack opening displacement profiles were measured, profiles along x direction (see Figure 1) in mid-thickness of all samples were selected and crack opening displacements along these profiles were extracted. The opening displacements were normalised by the crack opening displacement at the tip of the notch and the distance from the notch tip was normalised by the crack length from the notch tip as measured by phase congruency code. The results can be seen in Figure 6.

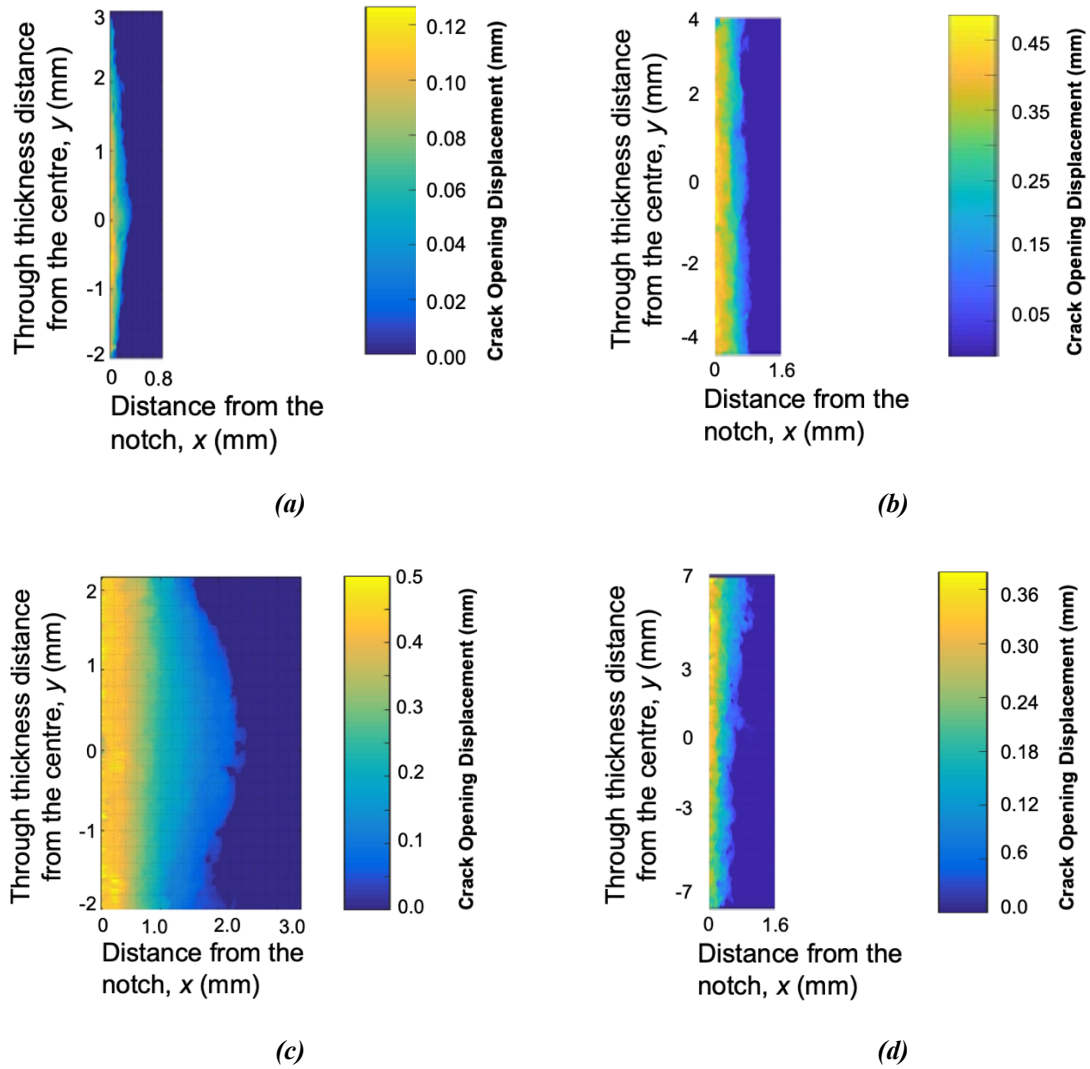

Figure 5: Mode I Crack opening displacement (a) thin – short (b) thick short (c) thin long (d) thick long. The crack opening displacements shown are calculated at the fracture load of each specimen, see Table 1.

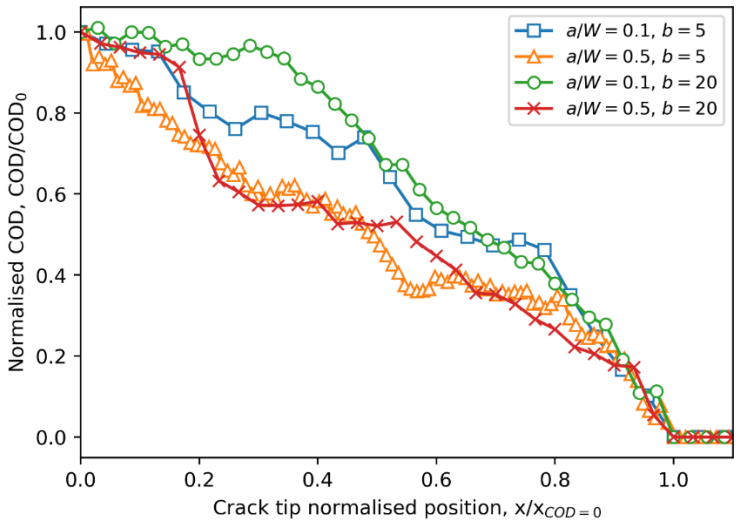

Figure 6: Normalised crack opening displacement profiles measured along the mid-thickness of each specimen at fracture.

2.4 *J*-integral calculation

A previously developed code [65][66], was used to calculate the energy release rate as a *J*-integral, from the displacement fields. The details can be found elsewhere [67]; in brief, the code creates a finite element mesh corresponding to the interrogation volumes at the final pass of the DVC analysis. It uses the geometry of the crack identified by phase congruency [68] to introduce a planar discontinuity in the mesh (i.e. two adjacent elements with nodes that are not tied together and can freely displace). It then reads the full-field displacement on every node in the model as boundary conditions. This creates an over-constrained finite element model, utilising Abaqus to calculate the strain field and the pre-defined constitutive law to calculate stress. Since the displacement field calculated by DVC near a discontinuity is not accurate [69][65], the code omits the DVC displacement field around the crack and allow the FE to solve for the displacement field in that region. Finally, it uses Abaqus' built in contour integral method to calculate the energy release rate associated with the crack. It is important to note that this analysis uses no information regarding the specimen dimensions, crack length or applied load. The current code uses two-dimensional plane strain/plane stress linear reduced integration elements (CPE4R) and imports the displacement field calculated by DVC slice by slice thus the volume of the simulation depends on the dimensions of the dataset. While this is a valid assumption for the surface (if plane stress elements are used) and middle of the specimens (if plane strain elements are used), it ignores the displacement field in the third direction (along the thickness) which could cause considerable error in the calculation of *J*-integral where plane strain or plane stress do not prevail. This point will be further discussed in the discussion section. It should be also noted that even the 20 mm thick specimens do not satisfy the ASTM E399 plane strain condition (i.e. $b>2.5(K_I/\sigma_o)^2$) as the minimum thickness dictated by the condition is above 350 mm which makes the X-ray penetration impossible.

The analysis used the material properties measured in section 2.1 and plane strain elements to represent the centre of the specimens. It used 20 contours around the crack tip for every virtual slice to ensure path independency of measured *J*-integrals. In all cases the values converged within the first 10 contours. The results for the *J*-integral were converted to K_J as per (Eq. 8):

$$K_J = \sqrt{\frac{JE}{1-\nu^2}} \qquad \text{(Eq. 8)}$$

Figure 7 shows the variation of K_J^{exp} through the normalised sample thickness. The thickness normalisation is carried out by the thickness through which *J* could be calculated x_0; that is, 5 mm and 4 mm for the thin sample with short and long cracks respectively (see Figure 5a and c) and 8 mm and 14 mm for the thick sample with short and long cracks respectively (see Figure 5b and d).

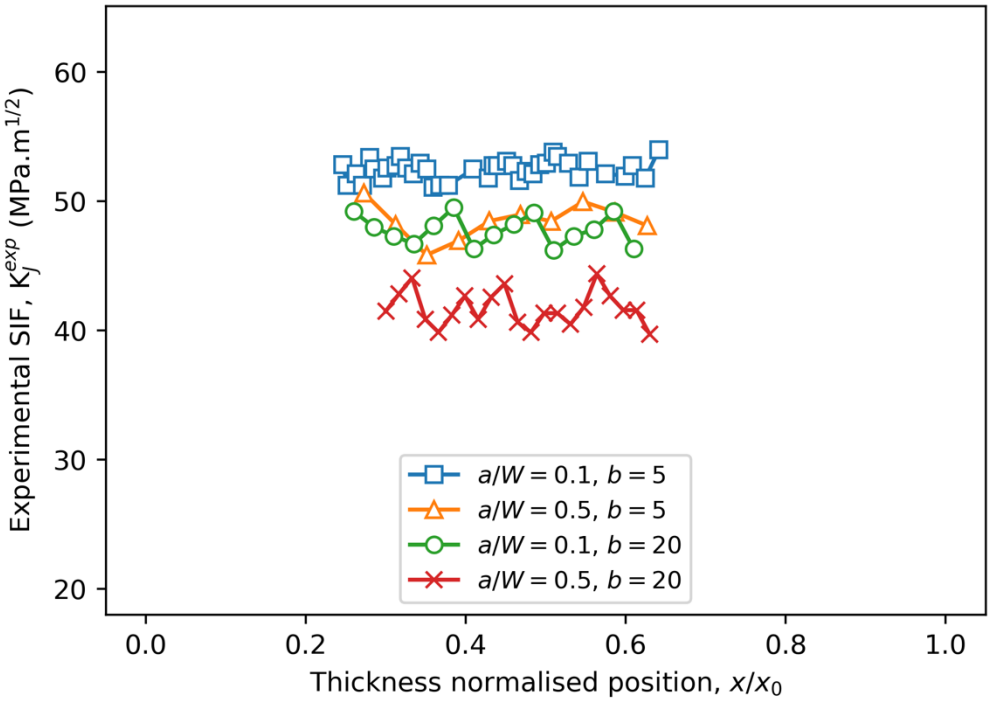

Figure 7: Experimentally measured stress intensity factor (SIF) plotted along the thickness of the sample by FE-DVC; typical error in K calculation estimated from the variation in K when contour independency was assumed to have been reached is 1.5 MPa.mm$^{1/2}$

3 Finite Element Modelling and Results

To independently validate and verify the stress intensity factors obtained in the previous section, three-dimensional finite element (3D FE) models of the experiments were created. It is important to note that in the previous section, the stress intensity factor was calculated using the displacement field measured and the measured material's constitutive law used to convert the strain to stress via DVC-FE. In the finite element analysis, on the other hand, the displacements were not used, rather the independently measured fracture force was exploited, using the material's constitutive law and specimen geometry to calculate the resultant displacements, strain field and stress field. It therefore can be argued that the two analyses are independent thus providing a robust validation route.

For the FE model, three-dimensional models of the four specimens were created using Abaqus 6.14 [70]. A 3D rigid body was created using 14,830 shell discrete rigid elements representing the loading fixture (see Figure 1a); the sample was made of 56,320 3D deformable linear solid elements CP20R. The seeds around the crack were 0.1 mm apart and 0.5 mm for the rest of the model. The mesh seeds were biased towards the curved blunted surface, but no degenerate elements were used at the crack tip. Two planes of symmetry were used to reduce the volume of the sample to a quarter of the actual size, x and y symmetry boundary conditions were enforced at the edges of the model. Each crack was modelled by removing the boundary conditions from the nodes along the notch of the sample. The effect of reduced stress singularity at the wire electro discharge machined notch (the samples were not pre-cracked) had to be included in the model. Without it, locally, the stress fields around the crack tips are unlikely to be accurate [71]. In order to allow for the effect of the blunt notch, the model had a notch radius of 0.05 mm, which allowed for the effect of the wire EDM to be considered. The crack was defined as a symmetry plane crack with a crack tip, on the line joining the curved blunted surface to the lower symmetry plane. The crack extension direction was perpendicular

to the surface of the notch [72]. The simulation used the same Ramberg – Osgood material model, as described in section 2.4. The model is shown in Figure 8 (the contour map shows the Von-Mises stress).

The rigid body's reference point was moved in displacement control and the applied displacement was iterated until its reaction force reached the experimental load that induced failure (given in Table 1) taking into account the symmetry planes defiled. The *J*-integral was calculated by defining a history output request; for the contour integral 20 contour integrals were used, the first of which was at the crack tip to ensure contour independency. The *J*-integrals, converted into equivalent stress intensity factors K_J^{FE} were extracted from all four models along the sample thickness; they can be seen in Figure 9: Stress intensity factor variation along the crack front of the four samples at the onset of fracture extracted from finite element simulations.. Also extracted was the length of plastic ligament in front of the crack tip, r_p. For this purpose, it was assumed that any point in front of the crack with von-Mises stress greater than the material yield stress (103 MPa) was plastic.

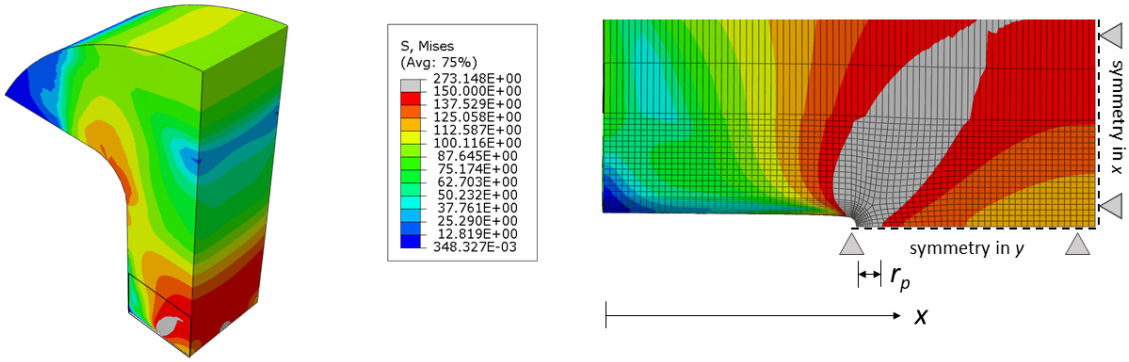

Figure 8: Finite element model of the thick sample with long crack (a) overview (b) details of the mesh at the crack tip - the grey colour shows the area in the model in which the material has deformed plastically

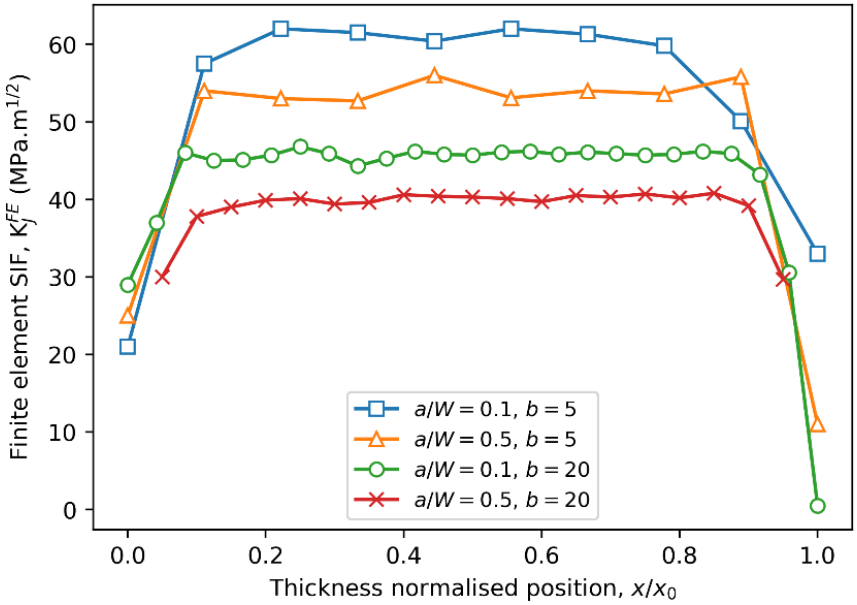

Figure 9: Stress intensity factor variation along the crack front of the four samples at the onset of fracture extracted from finite element simulations.

4 Discussion

Four specimens of a model material, an aluminium-titanium composite, with different levels of in and out-of-plane constraint were tested in this work. Tomograms of the specimens were recorded using synchrotron X-rays both before loading and at the onset of crack initiation from a sharp notch. DVC analysis of each pair of tomograms (before and after fracture) was possible due to attenuation contrast in the composite microstructure and revealed the full-field displacement field around the crack at equilibrium with the loading at the onset of fracture. Such analysis is currently not possible on more attenuating materials (e.g. uranium) and materials that do not have an inherent speckle pattern (e.g. stainless steel 316L). The displacement fields were used as an input in the finite element software, Abaqus, which calculated the corresponding strain fields at the crack. A tensile test was performed on the same material to extract its mechanical response, to which a Ramberg – Osgood constitutive law was fitted to the measured stress-strain response. The material constitutive law was used in the finite element models to enable the calculation of the stress field at the crack tip. A contour integral method, within Abaqus was then employed to calculate the through thickness *J*-integral at fracture initiation for the four levels of constraint; they are reported in Table 2. Q values for the four constraint conditions were calculated by subtracting the opening stress predicted by (σ_{yy}^{HRR}) for the opening stress at $x = 2J/\sigma_0$ from the model opening stress σ_{yy}^{FE} at the same location and normalising it the yield stress (σ_0); they are also reported in Table 2.

Independently, finite element models of the four specimens were created. The experimentally measured fracture loads were applied as boundary conditions to the models, using the same material constitutive law, and the through thickness *J*-integrals were calculated. The energy release rates calculated from analysis of the experiment and independent finite element simulation are compared in the form of equivalent stress intensity factor.

Table 2 – Equivalent stress intensity factor K_J (MPa.m$^{1/2}$)

Specimen	Experiment K_J^{Exp}		Finite element K_J^{FE}		
	Average	Standard deviation	Average	Standard deviation	Q
Thin - short	52.5	0.7	60.6	1.5	-0.67
Thin - long	48.6	1.3	54.0	1.2	-0.56
Thick - short	47.6	1.1	45.7	0.8	-1.29
Thick - long	41.7	1.3	39.9	0.7	-0.87

The experimentally extracted stress intensity factors and their variations across the thickness are reported in Table 2 along with the equivalent values extracted from the independent finite element models. In the table the values near the sample surface are discarded as the analysis was not valid in this region because the slice by slice treatment of the DVC slices assuming plane strain/plane stress condition loses the effects of out of plane displacement. It can be seen that the experimental and FE modelled average stress intensity factor in the middle of the specimen match well. However, by comparing Figure 7 and Figure 9 it is clear that towards the edge of the sample the values and trend of stress intensity factor in the FE and experiment

disagree. In the finite element model, the stress intensity factor decreases towards the surface, tending to zero at the surface as would be expected [73]. The experimental results suggest that the stress intensity factor increases towards the sample surface. There are two reasons for this discrepancy, one is that the code used to analyse the experimental data treats each virtual slice of material separately. This approach, while valid for the middle of the specimen, is not suitable for the variation of out-of-plane stress towards the surface. The solution to this issue is to develop an analysis code that creates a 3D DVC-FE model and reads the full volumetric DVC displacement in the model rather than slice by slice treatment that is used in the current version of the code. Secondly, it can be seen in Figure 5 that the cracks have tunnelled through the specimen and the crack front is bowed. This would tend to increase the stress intensity factor at the edges [74]; this is not modelled in the finite element simulation, which assumed a straight crack front.

Concentrating on the variation in stress intensity factor at the onset of fracture in the middle of the specimen, it can be seen that the highest value belongs to thin sample with short crack (52.5 ± 0.7 MPa.m$^{1/2}$) and lowest to the thick sample with long crack (41.7 ± 1.3 MPa.m$^{1/2}$). A comparison of equivalent stress intensity factor for the thick sample with a short crack (47.6 ± 1.1 MPa.m$^{1/2}$) or long crack (41.7 ± 1.3 MPa.m$^{1/2}$), against those in the thin samples with short crack (52.5 ± 0.7 MPa.m$^{1/2}$) or long crack (48.6 ± 1.3 MPa.m$^{1/2}$), shows the expected effect of loss of constraint i.e. thin samples have a higher toughness than thick samples and short cracks have higher toughness than samples with long cracks. The experimental values of equivalent stress intensity factor K_J^{exp} are plotted against their simulation counterpart K_J^{FE} in Figure 10. The figure shows the experimental and simulation value follow an acceptable one – one correlation providing confidence that the analyses are independent and are in good agreement.

Brittle fracture of materials is strongly dependent on the distribution of microstructural features such as microcracks and inclusions. As such, there is considerable variability in the toughness measured often instigating researchers to offer probabilistic distribution of toughness rather than the straightforward deterministic values. It therefore must be noted that testing 4 samples only may not provide the full picture of the toughness variability of the tested material. However, it is expected that there exists a correlation between the size of the plastic zone at the onset of fracture and the toughness measured. Therefore, it can be argued that despite the time constraints of a beamtime, which impose restrictions on the number of samples that can be fractured in-situ, the overall behaviour observed is consistent with the theoretical expectation of the variation in toughness as a function of combined in and out of plane constraint. However, the results of the current unique in-situ study must be seen in light of extensive ex-situ experimental programmes carried out previously to validate the Anderson – Dodds -Kirk unified measure of constraint.

The variation in toughness of brittle materials makes the experimental error estimation of utmost importance. There are two main outputs from the experiments, the toughness and the size of the plastic ligament, both calculated from the displacement measured by digital volume correlation analysis of the tomograms. The tomograms had of 3.3 and 7.9 micrometres voxel size for the thin and thick samples respectively. The tomograms were analysed by digital volume correlation with 16^3 and 8^3 interrogation window size for the thin and thick samples respectively. Previous investigation shows that DVC is accurate to 0.1 voxel at selected window sizes [75] resulting in an accuracy of roughly 0.3 and 0.8 micrometre in displacements measured from the thin and thick samples respectively. Considering the observable gauge length for each sample is the size of the interrogation window, the error in measured strain is of the order of 0.005 and 0.01 which at the worst case scenario (i.e. at yield stress) translates to 20 and 30 MPa uncertainty in measured stress for thin and thick samples. It can therefore be

argued that the error in measured plastic zone (accuracy of 0.3 and 0.8 for measurements between 3 and 400 micrometre) is negligible as is the error in measured toughness (accuracy of 0.2 and 0.3 measurements in 40 – 60 MPa.m$^{0.5}$). It was therefore concluded that the through thickness variation of the measured value are a good representation of the overall accuracy of the experimental measurements which are the values reported in Tables 2 and in Figures 10 - 12).

Figure 11 shows the equivalent stress intensity factors measured and calculated as a function of Q. As it can be seen, the variation of apparent stress intensity factor at different levels of constraint does not form a uniform trend. If applied to a constant thickness specimens (i.e. constant out of plane constraint), the results do form a trend but Q, in its original form, is evidently not capable of quantifying both in and out of plane at the same time. This has been previously observed by other researchers (e.g. see [38,40,48]).

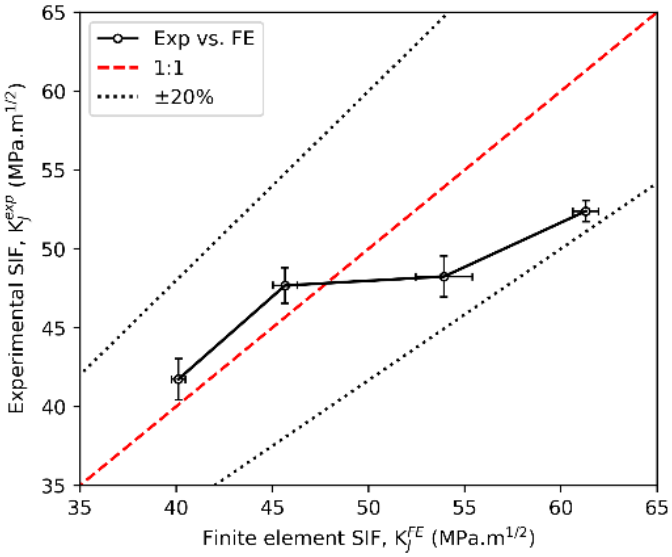

Figure 10: Correlation of experimentally obtained equivalent stress intensity factor and that of finite element simulation. A line highlighting a 1:1 correlation is shown, with all results falling within ±20% of this.

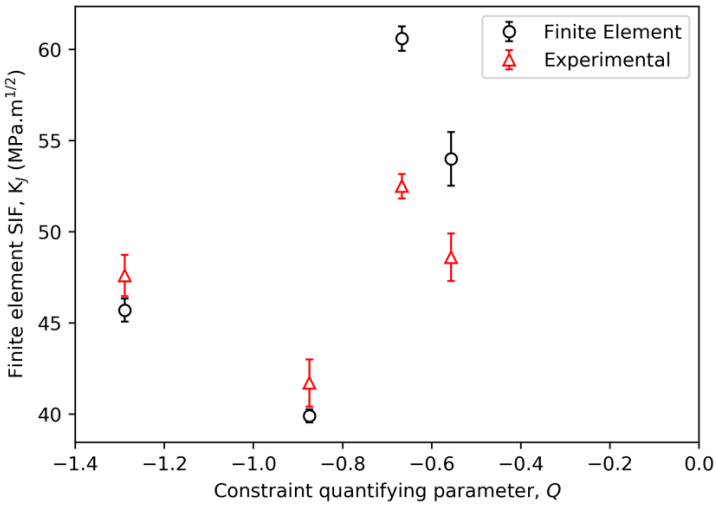

Figure 11: Stress intensity factor against measure of constraint Q. The error bar shows the range of values determined from experimental data and the measurement resolution (voxel size).

However, using a unified measure of constraint, it is possible to combine all the results by considering the relation between apparent stress intensity factors in the middle of sample. Figure 12 shows the apparent stress intensity factors measured/calculated in the middle of the specimens against a variation of Anderson, Dodds, and Kirk unified measure of constraint. In this variation, the Von Mises stress (σ_{vm}) was used instead of maximum principal stress (σ_1 - see Eq. 4) which had been originally proposed by Anderson, Dodds, and Kirk as it better represents the plastic work which is closely related to the constraint effect. This is in-line with previous work done by some of the authors (e.g. see [76]). If the arbitrary C factor in the modified Anderson. Dodds, Kirk model is considered to be one, then the unified measure of constrain would be the length of uncracked ligament which has deformed plastically is used. As noted by other researchers (e.g. see [40,48]), considering $C = 1$ restricts the application of such unified measure of constraint to conditions where the plastic zone size if limited within the sample. The thin specimens in this study had violated this condition as they had shown plastic deformation along the full uncracked ligament both in finite element model and in DVC. It was therefore decided to use a higher C factor (i.e. $C = 1.1$) to confine the area with Von-Mises stress bigger than $C\sigma_0$ within the specimen. The results are presented in Figure 12.

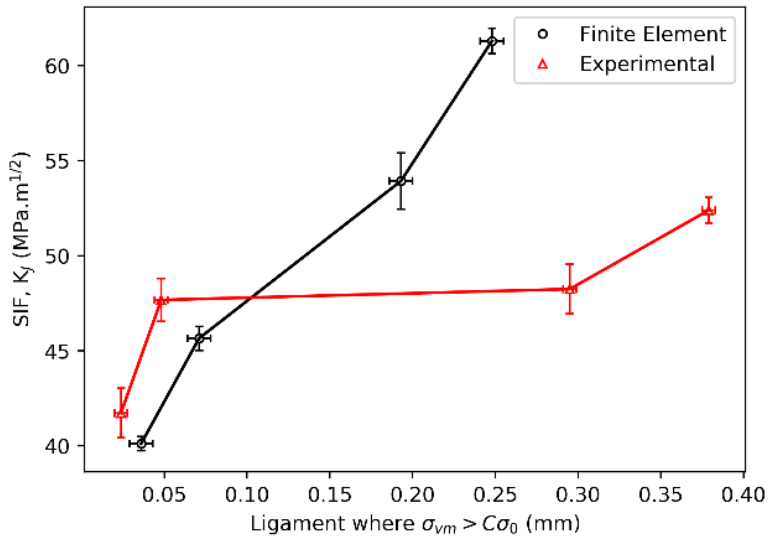

Figure 12: Stress intensity factor against a unified measure of constraint $C\sigma_0$ ($C = 1.1$). The error bar shows the range of values determined from experimental data and the measurement resolution (voxel size).

The figure shows that the apparent stress intensity factors plotted as a function of unified measure of constrain forms a uniform trend. The lowest constraint condition of thin sample with short crack show a large distance along the ligament with $\sigma_{vm} > 1.1\sigma_0$ while this distance is much smaller in the highest plastic constrain sample of thick with long crack. It appears that the FE results presented in Figure 12 are more in line with what is expected from the variation of toughness as a function of constraint compared to the experimental measurements. This is because the material has a low hardening exponent, expressing a near elastic – perfectly plastic behaviour. The elastic perfectly plastic behaviour results in large variation in strain as a function of small variation in stress (i.e. measured force over cross section). The large change in stress changes the finite element toughness variation considerably, exaggerating the effects of constraint and making the toughness increase as result of loss of constraint more prominent. This is not necessarily true representative of the material behaviour in service which is expected to be closer to the experimentally measured values. This is emphasising the importance of such direct measurements compared with previous theoretical studies.

Figure 12 suggests that using the unified measure of constraint can provide us with a relationship between combined in-plane and out-of-plane constraint level and equivalent stress intensity factor at fracture. This parameter to measure constraint can offer a methodology to include the effects of constraint in a prediction of fracture which is sensitive to both in and out-of-plane constraint. In future work we intend to use the experimentally measured displacement field to test the validity of other unified approaches, notably the Seal and Sherry method [44]. They have combined Rice and Tracey fracture model [43] with isostress contour method to produce a unified fracture criterion for a component with any thickness or crack length.

Conclusion

- Full-field volumetric displacement fields of four crack samples with four different combinations of in and out of plane constrains were measured by synchrotron X-ray tomography and digital volume correlation.
- The full-field volumetric displacement data were used in a finite element framework to calculate the through thickness energy release rate of the samples and the plastic zone sizes around the cracks at fracture.
- The plastic zone sizes at fracture were used to rank the samples constraint level regardless of their in or out of plane types. This showed, for the first time through direct measurement, that the size of plastic zone can be used as a unified measure of constraint.

Acknowledgement

SMT and MM would like to thank UK National Nuclear Laboratory for the financial support provided to carry out the work. Diamond Light Source is gratefully acknowledged the allocation of beamtime numbers EE12606-1 and EE12606-2. Drs S M Barhli and A Cinar are thanked for development of the codes that were used in the analysis of the DVC data. Professor Patrick Grant, University of Oxford is thanked for the provision of the material. We gratefully acknowledge the help and support of Dr Nghia Vo in the reconstruction of the limited angle tomography data. Mr R Patel, UK National Nuclear Laboratory and Dr A Wasylyk, Framatome, are gratefully acknowledged for their continuous and fruitful discussions.

Bibliography

[1] Cotterell B, Li QF, Zhang DZ, Mai YW. On the effect of plastic constraint on ductile tearing in a structural steel. Eng Fract Mech 1985.

[2] Henry BS, Luxmoore a. R. The stress triaxiality constraint and the Q-value as a ductile fracture parameter. Eng Fract Mech 1997.

[3] Brocks W, Schmitt W. The Second Parameter in *J*-R Curves: Constraint or Triaxiality ? In: Kirk M, Bakker A, editors. Constraint Eff. Fract. Theory Appl. Second Vol., West Conshohocken, PA: ASTM International; 1995, p. 209–31.

[4] Zhu XK, Chao YJ. Constraint effects on crack-tip fields in elastic-perfectly plastic materials. J Mech Phys Solids 2001;49:363–99.

[5] Yuan H, Brocks W. Quantification of constraint effects in elastic-plastic crack front fields. J Mech Phys Solids 1998;46:219–41.

[6] J., Zhao, W., Guo, C. S. The in-plane and out-of-plane stress constraint factors and K-

T-Tz description of stress field near the border of a semi-elliptical surface crack. International Journal of Fatigue 29 (2007) 435–443. n.d.

[7] Williams,M.L.: On the stress distribution at the base of a stationary crack. J. Appl. Mech. 24, 109–114 (1957) n.d.

[8] Omar, Bouledroua & Mohammed, hadj meliani & Guy, Pluvinage. (2016). A review of T-stress calculation methods in fracture mechanics computation. Nature Technologie. n.d.

[9] Zhao J, Guo W, She C, Meng B. Three dimensional K-Tzstress fields around the embedded center elliptical crack front in elastic plates. Acta Mech Sin Xuebao 2006.

[10] Williams ML. On the stress distribution at the base of a stationary crack. J Appl Mech 1957;24:109–114.

[11] Hancock J, Reuter W, Parks D. Constraint and toughness parameterized by T. ASTM STP 1171 Constraint Eff. Fract., 1993, p. 21–40.

[12] Larsson SG, Carlsson AJ. Influence of non-singular stress terms and specimen geometry on small-scale yielding at crack tips in elastic-plastic materials. J Mech Phys Solids 1973;21:263–77.

[13] Int J Fract, 114 (3) (2002), pp. 259-265Close SM. The influence of the T-stress on the directional stability of cracks. Int J Fract 2002;114:259–65.

[14] Gupta M, Alderliesten RC, Benedictus R. A review of T-stress and its effects in fracture mechanics. Eng Fract Mech 2015.

[15] Ayatollahi MR, Pavier MJ, Smith DJ. Mode I cracks subjected to large T-stresses. Int J Fract 2002;117:159–74.

[16] Hadj Meliani, M., Azari, Z., Pluvinage, G., Matvienko, Yu.G., The Effective T-stress Estimation and Crack Paths Emanating from U-notches, Engng Fracture Mechanics, Vol 77, Issue 11, July : 1682-1692, (2010). (PDF) A review of the influence of constraint o n.d.

[17] Larrosa NO, Ainsworth RA. Ductile fracture modelling and J-Q fracture mechanics: A constraint based fracture assessment approach. Frat Ed Integrita Strutt 2016.

[18] Betegón C, Hancock JW. Two-Parameter Characterization of Elastic-Plastic Crack-Tip Fields. J Appl Mech 1991.

[19] O'Dowd NP, Shih CF. Family of crack-tip fields characterized by a triaxiality parameter-I. Structure of fields. J Mech Phys Solids 1991.

[20] O'dowd NP. Applications of two parameter approaches in elastic-plastic fracture mechanics. Eng Fract Mech 1995.

[21] Hutchinson JW. Singular behaviour at the end of a tensile crack in a hardening material. J Mech Phys Solids 1968;16:13–31.

[22] Rice JR, Rosengren GF. Plane strain deformation near a crack tip in a power-law hardening material. J Mech Phys Solids 1968;16:1–12.

[23] Cravero S, Ruggieri C. Structural integrity analysis of axially cracked pipelines using conventional and constraint-modified failure assessment diagrams. Int J Press Vessel Pip 2006.

[24] Assessment of the integrity of structures containing defects', R6 Rev. 4, British Energy

Generation Ltd/BEG(UK)L, 2001. n.d.

[25] BS 7910: “Guide on methods for assessing the acceptability of flaws in fusion welded structures” (incorporating Amendment 1), BSI, 1999. n.d.

[26] Jin H.J., Wu S.J. Effect of plasticity constraint on structural integrity assessment of pressure vessel welds. Int. J. Pressure Vessels Pip. 2015;134:72–81. doi: 10.1016/j.ijpvp.2015.09.001. n.d.

[27] Zhu XKK, Jang SKK, Chen YFF. A Modification of J-Q Theory and Its Applications. Int J Fract 2001;111:47–52.

[28] Hancock JW, Reuter WG, Parks DM. Constraint and toughness parameterised by T. Constraint Effects in Fracture, , ed. American Society for Testing and Materials, Philadelphia, 1993,. In: Hackett EM, K.-H. S, Dodds. RH, editors. ASTM STP 1171, 1993.

[29] Hancock, J. W., Reuter, W. G. and Parks, D. M. C and toughness parameterised by TCE, in Fracture, ASTM STP 1171, ed. E. M. Hackett K-HS and RHDAS for T, and Materials, Philadelphia, 1993 pp. 21-40. No Title n.d.

[30] Kim Y, Zhu XK, Chao YJ. Quantification of constraint on elastic–plastic 3D crack front by the J–A2 three-term solution. Eng Fract Mech 2001;68:895–914.

[31] Zhang B, Guo W. Three-dimensional stress state around quarter-elliptical corner cracks in elastic plates subjected to uniform tension loading. Eng Fract Mech 2007.

[32] J., Zhao, Three-parameter approach for elastic–plastic stress field of an embedded elliptical crack. Engineering Fracture Mechanics 76 (2009) 2429–244. n.d.

[33] J., Zhao, W., Guo, Three-parameter K-T-Tz characterization of the crack-tip fields in compact-tension-shear specimens. Engineering Fracture Mechanics 92 (2012) 72–88. n.d.

[34] J., Zhao, W., Guo, C., She. The in-plane and out-of-plane stress constraint factors and K-T-Tz description of stress field near the border of a semi-elliptical surface crack. International Journal of Fatigue 29 (2007) 435–443. n.d.

[35] Dodds RH, Anderson TL, Kirk MT. A framework to correlate a/W ratio effects on elastic plastic fracture toughness. Int J Fract 1991;48:1–22.

[36] Anderson TL, Dodds RH, Wolfenden A, Anderson TL, Dodds RH. Specimen Size Requirements for Fracture Toughness Testing in the Transition Region. J Test Eval 1991;19:123–34.

[37] Mostafavi, M., Pavier, M. J. and Smith, D. J. (2009) Unified Measure of Constraint, ESIA10: Manchester, UK n.d.

[38] Mostafavi M, Smith DJ, Pavier MJ. Reduction of measured toughness due to out-of-plane constraint in ductile fracture of aluminium alloy specimens. Fatigue Fract Eng Mater Struct 2010;33.

[39] Mostafavi M, Pavier MJ, Smith DJ. Unified Measure of Constraint. Eng. Struct. Integr. Adv., Manchester, UK: 2010.

[40] Yang J, Wang GZ, Xuan FZ, Tu ST. Unified characterization of in-plane and out-of-plane constraint based on crack-tip equivalent plastic strain. Fatigue Fract Eng Mater Struct 2012;36:504–14.

[41] Shlyannikov VN, Boychenko N V., Tumanov A V., Fernández-Canteli A. The elastic and plastic constraint parameters for three-dimensional problems. Eng Fract Mech 2014.

[42] Mu MY, Wang GZ, Tu ST, Xuan FZ. Three-dimensional analyses of in-plane and out-of-plane crack-tip constraint characterization for fracture specimens. Fatigue Fract Eng Mater Struct 2016;39:1461–76.

[43] Rice JR, Tracey DM. On the ductile enlargement of voids in triaxial stress fields. J Mech Phys Solids 1969;17:201–17.

[44] Seal CK, Sherry AH. Predicting the effect of constraint on cleavage and ductile fracture toughness using area contour toughness scaling. Eng Fract Mech 2017;186:347–67.

[45] Lv J, Yu L, Du W, Li Q. Theoretical approach of characterizing the crack-tip constraint effects associated with material's fracture toughness. Arch Appl Mech 2018;88:1637–56.

[46] Huang X, Liu Y, Huang X. New constraint parameters based on crack tip plastic zone: Theoretical derivations and effectiveness verification. Int J Solids Struct 2019.

[47] Xu JY, Wang GZ, Xuan FZ, Tu ST. Unified constraint parameter based on crack-tip opening displacement. Eng Fract Mech 2018;200:175–88.

[48] Mu MY, Wang GZ, Xuan FZ, Tu ST. Unified correlation of in-plane and out-of-plane constraints with cleavage fracture toughness. Theor Appl Fract Mech 2015;80:121–32.

[49] Yang J, Wang GZ, Xuan FZ, Tu ST. Unified correlation of in-plane and out-of-plane constraint with fracture resistance of a dissimilar metal welded joint. Eng Fract Mech 2014;115:296–307.

[50] Wang YH, Wang GZ, Tu ST, Xuan FZ. Ductile fracture prediction based on J-integral and unified constraint parameters for cracked pipes. Eng Fract Mech 2019;215:1–15.

[51] LaVision. DaVis 8 n.d.

[52] Mostafavi M, Smith DJ, Pavier MJ. Fracture of aluminium alloy 2024 under biaxial and triaxial loading. Eng Fract Mech 2011;78.

[53] Bay BK. Methods and applications of digital volume correlation. J Strain Anal Eng Des 2008;43:745–60.

[54] ASTM E8. ASTM International, ASTM E8 Standard Test Methods for Tension Testing of Metallic Materials 2015.

[55] Anderson TL. Fracture Mechanics: Fundamentals and Applications. vol. 58. 2012.

[56] Wilson CD, Mani P. Plastic J-integral calculations using the load separation method for the center cracked tension specimen. Eng Fract Mech 2002;69:887–98.

[57] Drakopoulos M, Connolley T, Reinhard C, Atwood R, Magdysyuk O, Vo N, et al. I12: the Joint Engineering, Environment and Processing (JEEP) beamline at Diamond Light Source. J Synchrotron Radiat 2015;22:828–38.

[58] Mayo SC, Miller PR, Wilkins SW, Davis TJ, Gao D, Gureyev TE, et al. Quantitative X-ray projection microscopy: phase-contrast and multi-spectral imaging. J Microsc 2002;207:79–96.

[59] Cinar AF, Barhli SM, Hollis D, Flansbjer M, Tomlinson RA, Marrow TJ, et al. An autonomous surface discontinuity detection and quantification method by digital image correlation and phase congruency. Opt Lasers Eng 2017;96.

[60] Dowd BA, Campbell GH, Marr RB, Nagarkar V V, Tipnis S V, Axe L, et al. Developments in synchrotron x-ray computed microtomography at the National Synchrotron Light Source. Proc.SPIE, vol. 3772, 1999.

[61] Gürsoy D, De Carlo F, Xiao X, Jacobsen C. TomoPy: a framework for the analysis of synchrotron~tomographic data. J Synchrotron Radiat 2014;21:1188–93.

[62] Vo NT, Atwood RC, Drakopoulos M. Superior techniques for eliminating ring artifacts in X-ray micro-tomography. Opt Express 2018;26:28396–412.

[63] Abdel-Qader I, Abudayyeh O, Kelly ME. Analysis of edge-detection techniques for crack identification in bridges. J Comput Civ Eng 2003;17:255–63.

[64] Cinar AF. Volumetric Phase Congruency 2019.

[65] Barhli SM, Mostafavi M, Cinar AF, Hollis D, Marrow TJ. J-Integral Calculation by Finite Element Processing of Measured Full-Field Surface Displacements. Exp Mech 2017;57.

[66] Barhli SM. OUR-OMA 2019.

[67] Barhli, S. M. (2017). Advanced quantitative analysis of crack fields, observed by 2D and 3D image correlation, volume correlation and diffraction mapping (PhD thesis). University of Oxford. n.d.

[68] Kovesi P. Phase congruency: A low-level image invariant. Psychol Res Forsch 2000;64:136–48.

[69] Barhli SM. Advanced quantitative analysis of crack fields, observed by 2D and 3D image correlation, volume correlation and diffraction mapping. University of Oxford., 2017.

[70] ABAQUS/Standard User's Manual, Version 6.9. / Smith, Michael. Providence, RI : Simulia, 2009. n.d.

[71] Simpson CA, Tonge S, Cinar A, Reinhard C, Marrow TJ, Mostafavi M. Validating 3D two-parameter fracture mechanics for structural integrity assessments. Procedia Struct Integr 2018;13:965–70.

[72] Tonge SM, Cinar AF, Simpson C, Reinhard C, Connolley T, Marrow TJ, et al. J-integral evaluation of ductile material using X-Ray Tomography and Digital Volume Correlation (DVC), Southampton: British Society for Strain Measurement (BSSM); 2018.

[73] Ruggieri C, Panontin TL, Dodds RH. Numerical modeling of ductile crack growth in 3-D using computational cell elements. Int J Fract 1996;82:67–95.

[74] Zhao LG, Tong J, Byrne J. Stress intensity factor K and the elastic T-stress for corner cracks. Int J Fract 2001;109:209–25.

[75] Mostafavi M, Collins DM, Cai B, Bradley R, Atwood RC, Reinhard C, et al. Yield behavior beneath hardness indentations in ductile metals, measured by three-dimensional computed X-ray tomography and digital volume correlation. Acta Mater 2015;82.

[76] Mostafavi M, Smith DJ, Pavier MJ. The effect of out-of-plane loading on the fracture of aluminium 2024. 12th Int. Conf. Fract. 2009, ICF-12, vol. 3, 2009.